

Interaction effects on topological phase transitions via numerically exact quantum Monte Carlo calculations

Hsiang-Hsuan Hung,¹ Victor Chua,^{1,2} Lei Wang,³ and Gregory A. Fiete¹

¹*Department of Physics, The University of Texas at Austin, Austin, Texas, 78712, USA*

²*Department of Physics, The University of Illinois at Urbana-Champaign, Illinois, 61801, USA*

³*Theoretische Physik, ETH Zurich, 8093 Zurich, Switzerland*

We theoretically study topological phase transitions in four generalized versions of the Kane-Mele-Hubbard model with up to 2×18^2 sites. All models are free of the fermion-sign problem allowing numerically exact quantum Monte Carlo (QMC) calculations to be performed to extremely low temperatures. We numerically compute the \mathbb{Z}_2 invariant and spin Chern number C_σ directly from the zero-frequency single-particle Green's functions, and study the topological phase transitions driven by the tight-binding parameters at different on-site interaction strengths. The \mathbb{Z}_2 invariant and spin Chern number, which are complementary to each other, characterize the topological phases and identify the critical points of topological phase transitions. Although the numerically determined phase boundaries are nearly identical for different system sizes, we find strong system-size dependence of the spin Chern number, where quantized values are only expected upon approaching the thermodynamic limit. For the Hubbard models we considered, the QMC results show that correlation effects lead to shifts in the phase boundaries relative to those in the non-interacting limit, without any spontaneously symmetry breaking. The interaction-induced shift is non-perturbative in the interactions and cannot be captured within a "simple" self-consistent calculation either, such as Hartree-Fock. Furthermore, our QMC calculations suggest that quantum fluctuations from interactions stabilize topological phases in systems where the one-body terms preserve the D_3 symmetry of the lattice, and destabilize topological phases when the one-body terms break the D_3 symmetry.

PACS numbers: 71.10.Fd, 71.70.Ej

I. INTRODUCTION

Electron interactions in topological insulators^{1–20} have been a topic of intense research in recent years.^{21–26} It is crucial to go beyond the mean-field level^{27–31} to capture important fluctuation effects originating in the electronic correlations, as this can be decisive in determining the phase.^{32–37} Exact diagonalization studies³⁸ are inhibited by significant finite-size effects,³⁹ though they are unbiased by any particular ansatz in the way mean-field theories are. In this work, we study correlation effects in topological insulators by considering the Kane-Mele-Hubbard model and several variants with numerically exact projective quantum Monte Carlo (QMC) calculations. Due to their particle-hole symmetry, these models are free of the fermion minus sign problem, and QMC simulations provide a great opportunity to study correlation effects in topological matter with an unbiased theoretical approach. We are able to accurately treat correlations^{33,40}, compute interacting topological invariants such as the \mathbb{Z}_2 invariant and spin Chern number, and identify topological phase transitions through the zero-frequency single-particle Green's function.^{41,42} We thus avoid complications associated with ground-state evolution under twisted boundary conditions,⁴³ where numerical computations of a manifold ground states is required, and potential subtleties regarding energy gap closures must be addressed.⁴⁴

Strictly speaking, the ground state is altered when twisted boundary conditions are introduced. The existence of a family of ground states smoothly connected to

one and another, and a finite spectral gap are required for the use of twisted boundary conditions. Meeting these conditions can be especially challenging when approaching a phase transition where excitation gaps can become very small. Moreover, the use of the twisted boundary conditions is not practical in large-scale simulations, such as QMC; hence current implementations of twisted boundary conditions in interacting models have mainly focused on small sizes where exact diagonalization techniques have been used.^{38,39} In addition, the initial use of twisted boundary conditions for defining the spin Chern number introduced edge effects, which initially cast doubt on its robustness as a bulk topological invariant.^{44–46}

Therefore, it is worth revisiting topological phase transitions from the point-of-view of spin Chern numbers, particularly in the context of systems with interactions and finite-size effects present. We observe in our numerical QMC results a dichotomy in the role of on-site Hubbard interactions: Depending on the underlying lattice symmetry, they favor either a topological or trivial phase. Although our results are only limited to the class of models with particle-hole symmetry and S^z conservation, they could be hints of a more general principle regarding the interplay between point-group symmetry and interactions.

The remainder of this paper is organized as follows. In Section II, we introduce the Kane-Mele model and the four variants of it that we study. We compare and contrast the particular spatial symmetries exhibited by these toy models. In Section III, we follow up with a discussion

on the time-reversal invariant topological \mathbb{Z}_2 index and the spin Chern number with a focus on their numerical implementation in the presence of interactions. Next in Section IV which is the main part of our work, we present computations of topological indices in the presence intermediately strong interactions for the models introduced in Section II. This is followed up with discussions, interpretation, and speculation regarding these results in Section V. Then in Section VI we conclude with a summary and conclusions. Also included in the appendices are details regarding our quantum Monte Carlo methodology and supporting numerical results on the spin Chern number.

II. THE KANE-MELE MODEL AND SEVERAL VARIANTS

The Kane-Mele (KM) model, an early model supporting a \mathbb{Z}_2 topological insulator (TI) on the honeycomb lattice,^{47,48} remains central to the study of interaction effects in TI. The honeycomb lattice is a Bravais (triangular) lattice with a two-point basis (labeled as A and B). The vectors connecting two neighboring sites are $\mathbf{a}_{1,2} = \pm \frac{\sqrt{3}}{2}a\hat{x} + \frac{1}{2}a\hat{y}$ and $\mathbf{a}_3 = -a\hat{y}$, where a is the lattice constant between two nearest-neighbor sites as shown in Fig. 1 (a); we set $a = 1$ hereafter. The Hamiltonian reads as

$$H_{KM} = -t \sum_{\langle i,j \rangle} \sum_{\sigma} c_{i\sigma}^{\dagger} c_{j\sigma} + i\lambda_{SO} \sum_{\langle\langle i,j \rangle\rangle} \sum_{\sigma} \sigma c_{i\sigma}^{\dagger} \nu_{ij} c_{j\sigma},$$

where $c_{i\sigma}^{\dagger}$ ($c_{i\sigma}$) creates (annihilates) a spin σ fermion on site i and σ runs over \uparrow and \downarrow . Here, $\langle\langle \dots \rangle\rangle$ denotes second-neighbor terms given by vectors $\mathbf{b}_1 = \mathbf{a}_2 - \mathbf{a}_3$, $\mathbf{b}_2 = \mathbf{a}_3 - \mathbf{a}_1$ and $\mathbf{b}_3 = \mathbf{a}_1 - \mathbf{a}_2$ describing the spin-orbit coupling λ_{SO} . $i = 1, 2, 3$, and $\nu_{ij} = 1$ for counter-clockwise hopping and $\nu_{ij} = -1$ otherwise.⁴⁷

For our numerical study, we consider *four* time-reversal symmetric model Hamiltonians which are KM model-like: (i) the generalized Kane-Mele (GKM) model, the KM model with a spin-independent real-valued third-neighbor hopping term, (ii) the dimerized Kane-Mele (DKM), the KM model with a biased nearest-neighbor hopping along the \mathbf{a}_1 direction, (iii) the t_L -KM model, the KM model with 5-th neighbor hopping, and (iv) the t_{3N} -dimerized KM model, which is a hybrid of model (i) and (ii).

All of the models are generalized versions of the KM models, and at half-filling, they preserve the particle-hole symmetry. In the non-interacting limit, they host a topological-insulator/trivial insulator phase transition by tuning tight-binding parameters. However, there exists crucial differences among the models. The GKM model (i) and the t_L -KM model (iii) preserve the six-fold rotation or C_6 symmetry of the honeycomb lattice, whereas the DKM model (ii) and the t_{3N} -dimerized model (iv) explicitly break it down to C_2 with the bias in the \mathbf{a}_1

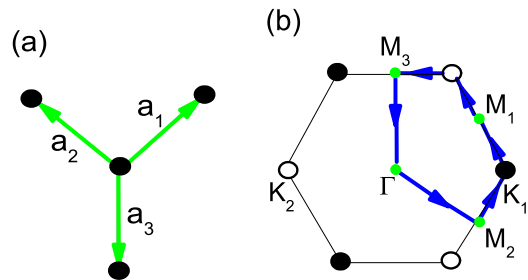


FIG. 1. (Color online) (a) The honeycomb lattice and the underlying vectors $\mathbf{a}_{1,2,3}$. (b) The first Brillouin zone of the honeycomb lattice. The Dirac points are $K_{1,2} = (\pm \frac{4\pi}{3\sqrt{3}a}, 0)$ labeled by open and solid circles, respectively. The time-reversal invariant momentum (TRIM) points labeled by the green dots are $\Gamma = (0, 0)$ and $M_{1,2} = (\pm \frac{\pi}{\sqrt{3}a}, \frac{\pi}{3a})$ and $M_3 = (0, \frac{2\pi}{3a})$.

direction. In the following we will mainly focus on the GKM and DKM models.

The wallpaper or 2D space group of the honeycomb lattice is $\mathbf{p6m}$ which is *symmorphic* and has D_6 as its point group. The different models considered are meant to represent different modifications of the bare KM model such that the D_6 symmetry is either preserved or broken but which nevertheless exhibits a topological insulator phase transition. However, time-reversal, spin- S^z , inversion, and particle hole symmetry are preserved in all these models. More precisely these models exhibit the Quantum Spin Hall (QSH) phase when topologically non-trivial under the \mathbb{Z}_2 classification of 2D time-reversal symmetric topological insulators. It is well known that the KM model includes spin-orbit coupling in the form of spin-dependent second nearest neighbor hopping that favors the topological insulator phase. We shall see in models (i-iv) that hoppings which are additions to the standard KM model will, at sufficient strengths, overcome this tendency of the spin-orbit coupling and stabilize the trivial phase without breaking any symmetries.

Resuming our discussion on symmetry, recall that $D_6 \cong D_3 \times \mathbb{Z}_2^{(i)}$, where the (i) superscript in $\mathbb{Z}_2^{(i)}$ denotes 2D inversion about the center of the hexagon. Furthermore $D_3 \cong C_3 \times \mathbb{Z}_2^{(m)}$ where the (m) denotes reflection about a vertical mirror plane i.e. $\mathbb{Z}_2^{(m)} \equiv \sigma_v$ in Schönflies notation. Moreover, in two dimensions inversion is isomorphic to rotation by 180° or $\mathbb{Z}_2^{(i)} \cong C_2$. Models (i-iv) are selected to maintain $\mathbb{Z}_2^{(i)}$ inversion symmetry but may either preserve or break D_3 down to $\mathbb{Z}_2^{(m)}$ or completely. A further essential property that is common to these models is the absence of QMC sign problems in their respective Hubbard model incarnations, which are obtained by the inclusion of an on-site Hubbard interaction.

Specializing to two dimensions, the seminal works of Kane and Mele^{47,48}, and later Bernevig *et. al.*⁴⁹, Schnyder *et. al.*⁵⁰, Kitaev,⁵¹ and Qi *et. al.*⁵² showed that with

only time-reversal symmetry the non-interacting topological phases are classified by a \mathbb{Z}_2 invariant, which is also generalized to three dimensions by Fu and Kane⁵³, and Moore and Balents⁵⁴. The physical content of this binary topological index is that it enumerates the number parity of Kramers pairs of gapless edge modes at a boundary of the system with the vacuum—at least for non-interacting gapped band insulators. With the absence of S^z mixing, the non-interacting occupied bands may be further categorized by their S^z polarization, and each spin species is topologically non-trivial carrying a non-zero integral Chern number; *i.e.* $C_\sigma \neq 0$, $\sigma = \uparrow, \downarrow$.⁵⁵ However, due to time-reversal symmetry, $C_\uparrow + C_\downarrow = 0$, and hence we do not expect an Integer Quantum Hall effect. Nevertheless, if the spin Chern number^{46,56,57} defined by

$$C_{\text{spin}} = \frac{C_\uparrow - C_\downarrow}{2} = C_\uparrow = -C_\downarrow \quad (1)$$

is odd and non-zero, then the ground state of filled bands are in the non-trivial topological insulator phase or the \mathbb{Z}_2 odd phase. The non-mixing of S^z sectors, designates this non-trivial phase as being the QSH phase where on the edge, an odd number of helical edge states carrying S^z -current persists so long as time-reversal symmetry and the bulk band gap are preserved. As was stated, all the models we have considered will either be trivial or in the QSH phase in the non-interacting limits. In this work, we will demonstrate that the classification by C_{spin} will not only be applicable in the non-interacting limit, but can also be extended to finite interaction where our main interests lie. It is also clear that under this classification, a topological phase transition between even and odd values of C_{spin} must proceed by an odd variation $\Delta C_{\text{spin}} \in 2\mathbb{Z} + 1$.

It will be highlighted in the upcoming sections that crystal symmetry will play a crucial role in the nature of such topological transitions.

(i) Generalized Kane-Mele model

We start with the GKM model previously introduced in Ref.[33] whose Hamiltonian is given by

$$H_{GKM} = -t \sum_{\langle i,j \rangle} \sum_{\sigma} c_{i\sigma}^\dagger c_{j\sigma} + i\lambda_{SO} \sum_{\langle\langle i,j \rangle\rangle} \sum_{\sigma} \sigma c_{i\sigma}^\dagger \nu_{ij} c_{j\sigma} - t_{3N} \sum_{\langle\langle\langle i,j \rangle\rangle\rangle} \sum_{\sigma} c_{i\sigma}^\dagger c_{j\sigma}, \quad (2)$$

where $\langle\langle\langle \dots \rangle\rangle\rangle$ third-neighbor terms, and the vectors connecting third-neighbor terms are given by $\mathbf{c}_i = \mathbf{a}_i + \mathbf{b}_i$. At $t_{3N} = 0$ and finite spin-orbit coupling λ_{SO} , the model Hamiltonian Eq. (2) is reduced to the Kane-Mele model,^{47,48} which is a two-dimensional \mathbb{Z}_2 topological insulator.⁴⁷⁻⁴⁹ Like the KM model, the GKM model is invariant under both the time-reversal symmetry and the honeycomb space group $p6m$ symmetry with its point group D_6 .

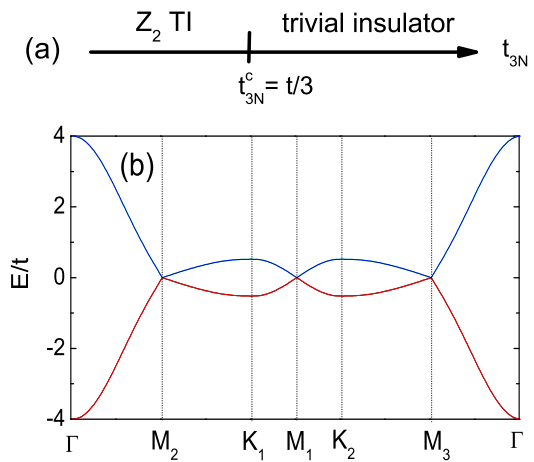


FIG. 2. (Color online) (a) Schematic phase diagram of the GKM model. (b) The noninteracting band structure of the GKM model at $t_{3N}^c = \frac{1}{3}t$ (here using $\lambda_{SO} = 0.1t$). The presented momenta are chosen along the path depicted as blue arrows in Fig. 1 (b). The gap closes at three TRIM points: $M_{1,2,3}$, instead of the Dirac point $K_{1,2}$.

In the large t_{3N} limit of Eq. (2), the system is a trivial insulator, implying the GKM model undergoes a symmetry-preserving topological phase transition as a function of t_{3N} .³³ The GKM model can be recast as $H_{GKM} = \sum_{\mathbf{k}} \Phi_{\mathbf{k}}^\dagger H_{\mathbf{k}}^{GKM} \Phi_{\mathbf{k}}$, where $\Phi_{\mathbf{k}} = (c_{A\uparrow\mathbf{k}}, c_{B\uparrow\mathbf{k}}, c_{A\downarrow\mathbf{k}}, c_{B\downarrow\mathbf{k}})$ is a 4-component spinor and $H_{\mathbf{k}}$ reads

$$H_{\mathbf{k}}^{GKM} = \begin{pmatrix} f(\mathbf{k}) & h(\mathbf{k}) \\ h^*(\mathbf{k}) & -f(\mathbf{k}) \\ & -f(\mathbf{k}) & h(\mathbf{k}) \\ & h^*(\mathbf{k}) & f(\mathbf{k}) \end{pmatrix},$$

where $h(\mathbf{k}) = g(\mathbf{k}) - t_{3N} \sum_i e^{i\mathbf{k} \cdot \mathbf{c}_i}$; $g(\mathbf{k}) = -t \sum_i e^{i\mathbf{k} \cdot \mathbf{a}_i}$, and $f(\mathbf{k}) = 2\lambda_{SO} \sum_i \sin(\mathbf{k} \cdot \mathbf{b}_i)$; note that \mathbf{a}_i , \mathbf{b}_i and \mathbf{c}_i are real-space vectors to describe nearest, second and third-neighbor hoppings. For most t_{3N} values, the GKM model is gapped. However a simple analysis of the dispersion will show a gap closure at $t_{3N}^c = \frac{1}{3}t$ independent of λ_{SO} , and permits a change in the topological \mathbb{Z}_2 index. The schematic phase diagram is shown in Fig. 2 (a). For $t_{3N} < t_{3N}^c$, the system is a \mathbb{Z}_2 TI, whereas for $t_{3N} > t_{3N}^c$, the system is a trivial insulator. Thus, there exists a topological phase transition at $t_{3N} = \frac{1}{3}t$.

The non-interacting band structure of the GKM model is depicted in Fig. 2 (b). The chosen momenta are along the high symmetry momentum lines as indicated arrows in Fig. 1 (b). Of particular note is the C_6 symmetry of the dispersion that relates the three high-symmetry $M_{1,2,3}$ points which are also inversion symmetric points. These become *three* Dirac points at the critical topological phase transition; gaps are opened at $K_{1,2}$ due to the spin-orbit coupling λ_{SO} . One should contrast the topological phase transition with the KM model, which involves *two* Dirac nodes at the K_1 and K_2 points. Note that at $t_{3N} = t/3$ and $\lambda = 0$, the bands still touch at

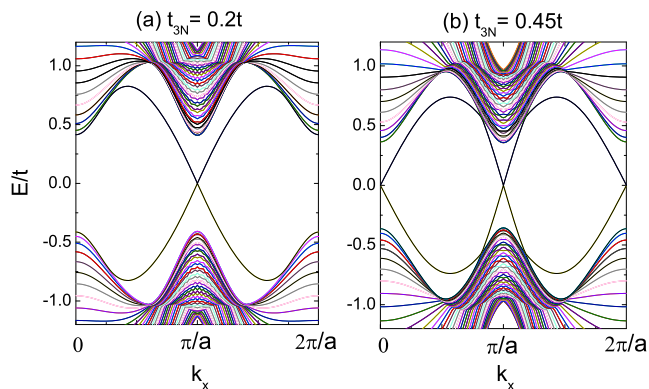


FIG. 3. (Color online) The edge spectra for the noninteracting GKM model at $\lambda_{SO} = 0.2t$ and (a) $t_{3N} = 0.2t$, a \mathbb{Z}_2 topological insulator and (b) $t_{3N} = 0.45t$, a trivial insulator. A ribbon geometry is used with an armchair edge for periodic boundary conditions (length, x -direction) and zigzag edge for open boundary conditions (width).

the $M_{1,2,3}$ points as well as at the $K_{1,2}$ points, yielding 5 Dirac points.

Displayed in Fig. 3 are results of a band structure computation in a strip geometry of the GKM model demonstrating the existence of edge states with energies that traverses the bulk energy gap. By counting the number of Kramers pairs of edge states per edge,^{47,48} we note that the GKM model undergoes a topological phase transition as a function of t_{3N} , whereby an odd number of Kramers pairs characteristic of a \mathbb{Z}_2 topological insulator phase turns into an even number characteristic of a topologically trivial phase.^{47,48} Although the two pairs of Kramers helical states in Fig. 3(b) shows that the GKM model at $t > t_{3N}^c$ is a \mathbb{Z}_2 trivial insulator,³³ for each spin flavor the spin Chern number, C_σ is even and nonzero. Namely, $|C_\sigma| = 2 \neq 0$ implying nontrivial edge states,⁵⁸ albeit ones not protected by time-reversal symmetry. In addition, since the bulk gap of the GKM model closes at the *three* time-reversal invariant momenta: M_1 , M_2 and M_3 [in Fig. 2 (b)], we expect that the spin Chern number will suffer an *odd* variation⁵⁹ $|\Delta C_\sigma| = 3$ signaling a topological transition from the $C_\sigma = \pm 1$ state to the $C_\sigma = \mp 2$ state for spin-up and spin-down fermions, respectively.

Note that the appearance of these three Dirac cones, each carrying unit Berry monopole charge, is mandated by the C_3 crystal symmetry, since M_1, M_2, M_3 transform amongst themselves in a non-trivial irreducible representation of the unbroken C_3 symmetry. It must be mentioned that a topological transition with ΔC_σ odd may also involve an *even* number of Dirac cones as is the case as in the KM model where a staggered AB -site potential competes with spin-orbit coupling. In this instance, however, the inversion symmetry is broken from the pristine graphene band structure allowing the transfer of an odd amount of Chern number. This is because under broken inversion symmetry, the K_1 and K_2 are not required

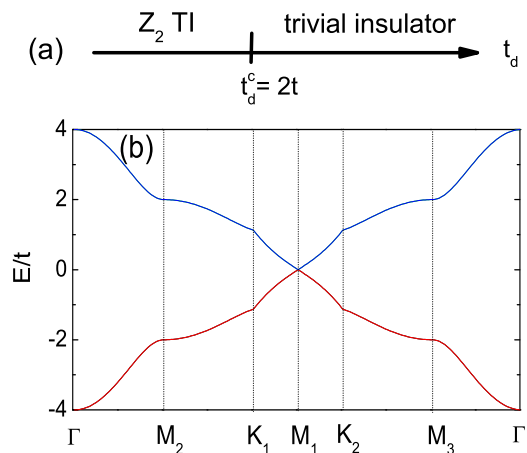


FIG. 4. (Color online) (a) Schematic phase diagram of the DKM model. (b) The noninteracting band structure of the DKM model at $t_d^c = 2t$ (here using $\lambda_{SO} = 0.1t$). The presented momenta are chosen along the path depicted as blue arrows in Fig. 1 (b). The gap closes at one TRIM point: M_1 , instead of the Dirac point $K_{1,2}$. Compare with Fig.2.

to contribute equally in the transfer of Chern number. The GKM model, however, differs by always maintaining inversion symmetry and in fact the M points are individually inversion symmetric points. Lastly, from the perspective of the spin Chern numbers, both phases are nontrivial—they exhibit edge robust states so long as S^z symmetry is preserved, and are classified by the spin Chern number.^{56,57}

(ii) Dimerized Kane-Mele model

The second model we consider, the DKM model is expressed by the following Hamiltonian⁴⁰

$$H_{DKM} = - \sum_{\langle i,j \rangle} \sum_{\sigma} t_{ij} c_{i\sigma}^{\dagger} c_{j\sigma} + i\lambda_{SO} \sum_{\langle\langle i,j \rangle\rangle} \sum_{\sigma} \sigma c_{i\sigma}^{\dagger} \nu_{ij} c_{j\sigma}, \quad (3)$$

where $t_{ij} = t_d$ when $\mathbf{r}_j = \mathbf{r}_i + \mathbf{a}_1$, whereas $t_{ij} = t$ otherwise. One can recast the Hamiltonian as $H_{DKM} = \sum_{\mathbf{k}} \Phi_{\mathbf{k}}^{\dagger} H_{\mathbf{k}}^{DKM} \Phi_{\mathbf{k}}$, where $H_{\mathbf{k}}$ is

$$H_{\mathbf{k}}^{DKM} = \begin{pmatrix} f(\mathbf{k}) & h'(\mathbf{k}) \\ h'(\mathbf{k})^* & -f(\mathbf{k}) \\ & -f(\mathbf{k}) & h'(\mathbf{k}) \\ & h'(\mathbf{k})^* & f(\mathbf{k}) \end{pmatrix},$$

where $h'(\mathbf{k}) = -t_d e^{i\mathbf{k} \cdot \mathbf{a}_1} - t \sum_{i=2,3} e^{i\mathbf{k} \cdot \mathbf{a}_i}$. At $t_d = t$, Eq. (3) is reduced to the KM model. This kinetic Hamiltonian explicitly breaks the C_3 subgroup of D_6 resulting in the point group $\mathbb{Z}_2^{(m)} \times \mathbb{Z}_2^{(i)}$ which is a mirror reflection perpendicular to \mathbf{a}_1 and inversion or 180° rotation. A schematic of its phase diagram and band structure at the critical point are shown in Fig. 4.

A topological phase transition will occur by tuning t_d to twice the nearest-neighbor hopping. In this instance

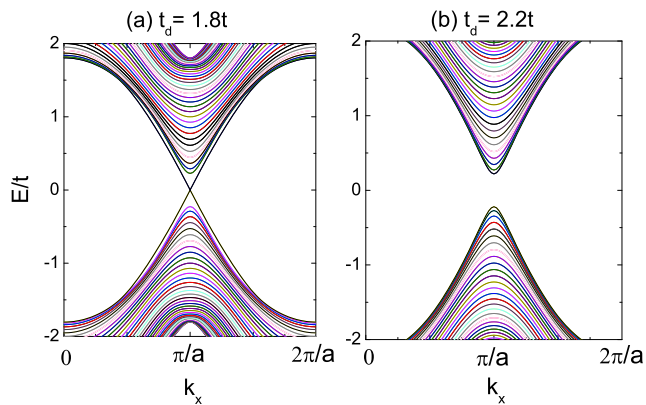


FIG. 5. (Color online) The edge spectra for the noninteracting DKM model at (a) $t_d = 1.8t$ and (b) $t_d = 2.2t$, for a \mathbb{Z}_2 topological insulator and a trivial insulator, respectively. $\lambda_{SO} = 0.2t$ is used. The anisotropic hopping t_d is introduced along the zigzag direction.

the conduction and valence bands touch at a *single* Dirac cone at the M_1 point when $t_d^c = 2t$ (again independent of the value of λ_{SO}). This critical point separates a trivial and the topological insulator phase, as shown in Fig. 4.⁴⁰ In Fig. 5 we show the band structure in a strip geometry for the DKM model. The topological phase transition in the DKM model, however, is different from the one in the GKM model as noted by the absence of any helical edge modes on the trivial insulator side [shown in Fig. 5(b)]. Thus, the trivial insulator phase ($t_d > t_d^c$) has zero spin Chern number and its variation is $|\Delta C_\sigma| = 1$ during the topological phase transition.

From the symmetry perspective, the transition in the DKM model greatly differs from the GKM model since C_3 is completely broken leaving only mirror and inversion $\mathbb{Z}_2^{(m)} \times \mathbb{Z}_2^{(i)}$ symmetries of the original D_6 point group. Besides the trivial Γ point, the M_1 point – where the *single* critical Dirac cone appears – is the only inversion symmetric point which also respects the residual mirror symmetry. Thus, the topological phase transition proceeds as a unit change of spin Chern number and hence the topological \mathbb{Z}_2 index. In summary, we see that at least in the non-interacting limit, point group symmetry can greatly influence the form of the electronic structure of the critical point straddling a QSH phase and trivial phase.

(iii) t_L Kane-Mele model

The next model on our list is the t_L -KM model which supplements the KM model with a four-lattice-constant-range hopping of strength t_L . Similar to the t_{3N} term in the GKM model, the tight-binding parameter, t_L , in the t_L -KM model preserves the D_6 point group symmetry of

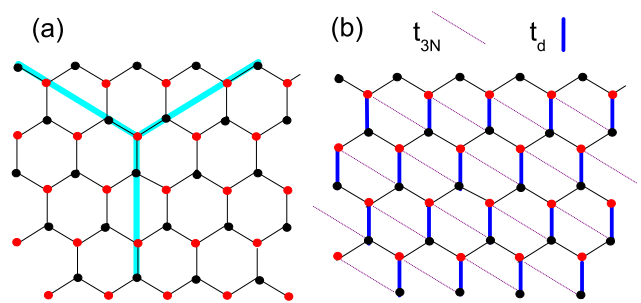


FIG. 6. (Color online) (a) The t_L -KM model and (b) The t_{3N} -dimerized KM model.

the honeycomb lattice. The model Hamiltonian reads as

$$H_{t_L} = -t \sum_{\langle i,j \rangle} \sum_{\sigma} c_{i\sigma}^\dagger c_{j\sigma} + i\lambda_{SO} \sum_{\langle\langle i,j \rangle\rangle} \sum_{\sigma} \sigma c_{i\sigma}^\dagger \nu_{ij} c_{j\sigma} - t_L \sum_{\{i,j\}} \sum_{\sigma} c_{i\sigma}^\dagger c_{j\sigma}, \quad (4)$$

where the first two terms describe the KM model, and in the third term $\{i,j\}$ denotes the *real-valued* hopping with the distance of $4a$. The lattice structure is shown in Fig. 6 (a). Similar to the GKM model, in the non-interacting limit, there exists a topological phase transition from the \mathbb{Z}_2 topological insulator to the trivial insulator state. In this instance, the boundary is located at $t_L = \frac{1}{3}t$ with three M_1, M_2, M_3 Dirac cones. For simplicity, we do not discuss the properties of the edge dispersion as they are qualitatively similar to the GKM model.

(iv) t_{3N} -Dimerized Kane-Mele model

The final model we consider is the t_{3N} -dimerized KM model which is constructed by the combination of one third-neighbor hopping (instead of three) *and* the bond dimerization in the KM model. As shown in Fig. 6 (b), the solid blue lines denote the dimerized bonds with t_d strength and the purple dotted lines denote the diagonal t_{3N} hopping. The Hamiltonian reads as

$$H_{t_{3N}d} = - \sum_{\langle i,j \rangle} \sum_{\sigma} t_{ij} c_{i\sigma}^\dagger c_{j\sigma} + i\lambda_{SO} \sum_{\langle\langle i,j \rangle\rangle} \sum_{\sigma} \sigma c_{i\sigma}^\dagger \nu_{ij} c_{j\sigma} - t_{3N} \sum_{\{i,j\}=\mathbf{c}_3} \sum_{\sigma} c_{i\sigma}^\dagger c_{j\sigma}, \quad (5)$$

where $t_{ij} = t_d$ if $\mathbf{r}_j = \mathbf{r}_i + \mathbf{a}_3$; otherwise $t_{ij} = t$. The first two terms give the DKM model. The real-valued diagonal t_{3N} hopping is selected along $\mathbf{c}_3 = \sqrt{3}a\hat{x} - a\hat{y}$.

The simultaneous presence of the dimerized bonds and t_{3N} bonds breaks the $\mathbb{Z}_2^{(m)}$ mirror reflection and C_3 rotational symmetry of $D_6 \cong (C_3 \times \mathbb{Z}_2^{(m)}) \times \mathbb{Z}_2^{(i)}$. Thus the D_3 subgroup is completely broken, however the $\mathbb{Z}_2^{(i)}$ inversion symmetry is still respected. There also exists a topological phase transition between the \mathbb{Z}_2 topological insulator

state and the trivial state, and the non-interacting critical condition can be determined to be $t_{3N} + t_d = 2t$ which is again independent of the value of λ_{SO} . At the topological phase boundary, $t_d^c = 2t - t_{3N}$, the bands form a single Dirac cone at M_3 , which hints that the spin Chern number has changed by $|\Delta C_\sigma| = 1$ during the topological phase transition.

III. NUMERICAL EVALUATION OF TOPOLOGICAL INDICES

For each generalization or variant of the Kane-Mele model, an on-site Hubbard interaction will be added, and interacting phase diagrams containing the trivial and topological phases are obtained via QMC simulations. But first we review and discuss the quality of numerically computed topological indices of the finite clusters in the non-interacting limit.

The first and most important topological index is the \mathbb{Z}_2 invariant of a two-dimensional non-interacting topological insulator.⁴⁸ When inversion symmetry is present, the noninteracting \mathbb{Z}_2 invariant is determined as⁴⁵

$$(-1)^\nu = \prod_{\mathbf{k}_i \in \text{TRIM}} \prod_m \xi_{2m}(\mathbf{k}_i), \quad (6)$$

where $\xi_{2m}(\mathbf{k}_i)$ is the parity of $2m$ -th occupied Hamiltonian eigenstate at the time reversal invariant momentum (TRIM); in the KM models, they are Γ and $M_{1,2,3}$ as depicted in Fig. 1 (b). $(2m-1)$ -th and $2m$ -th states share the same parity and are a Kramers pair, and therefore should only be counted once in the determination of the topological invariant. The time-reversal invariant topological insulator phase is stable in the weakly interacting limit⁶⁰ and the \mathbb{Z}_2 index is also well defined in the case of weak-interactions. It may be obtained conveniently from the zero-frequency single-particle Green's function.^{41,42} Specialized to the presence of inversion symmetry, the Fu-Kane⁴⁵ expression Eq. (6) with interactions generalizes to

$$(-1)^\nu = \prod_{\mathbf{k}_i \in \text{TRIM}} \tilde{\eta}(\mathbf{k}_i), \quad (7)$$

where $\tilde{\eta}(\mathbf{k}_i)$ are the parity eigenvalues (one per Kramer's pair) of the R-zero^{41,61} eigenstates of the zero-frequency Green's functions at TRIM. R- and L-zeros are terms used to refer to eigenfunctions of the zero-frequency single particle Green's function $G_\sigma(i\omega = 0, k)$. Eigenfunctions $|v_{nk\sigma}\rangle$ with band index n , spin σ , crystal momentum k and eigenvalue such that

$$G_\sigma(i\omega = 0, k)|v_{nk\sigma}\rangle = \lambda_{nk\sigma}|v_{nk\sigma}\rangle \quad (8)$$

are called R-zeros when $\lambda_{nk\sigma} > 0$, and L-zeros when $\lambda_{nk\sigma} < 0$.⁴¹ In the non-interacting limit, R-zeros correspond to occupied states below the Fermi-energy. (Note that Eq.(8) is often expressed in terms of the *inverse* Green's function.⁴¹ Since our system consists of 2×2

matrices for each spin value, we can equivalently express the formula directly in terms of the Green's function. One need only exercise care in the meaning of L-zeros, R-zeros, and singularities of the Greens functions.) The singular case $G_\sigma(i\omega, k) \sim 1/\omega$ as $\omega \rightarrow 0$ corresponds to the presence of gapless quasiparticles where a gapped topological insulating phase is not well-defined. The interesting case of $G_\sigma(i\omega = 0, k) = 0^{62-64}$ or $\lambda_{nk\sigma} = 0$ is an indication of the onset of an interaction driven metal-insulator transition in the Brinkman-Rice sense.⁶⁵ Either a pole singularity or zero of $G_\sigma(i\omega = 0, k)$ may induce a change in the topological index. This expression for the $(-1)^\nu$ index is immensely useful and convenient in determining the topological phase of an interacting time-reversal invariant system, but is however limited to the inversion symmetric situations.

The second topological index that will concern us is the spin Chern number defined by Eq. (1) in the QSH context. The Chern numbers C_σ of the S^z projected bands are expressed in terms of one particle spectral projectors⁶⁶ as

$$C_\sigma = \frac{i}{2\pi} \int d^2k \epsilon^{\mu\nu} \text{Tr} [P_\sigma(k) \partial_\mu P_\sigma(k) \partial_\nu P_\sigma(k)], \quad (9)$$

where $P_\sigma(k) = \sum_n |v_{nk\sigma}\rangle \langle v_{nk\sigma}|$ is the single particle spectral projector onto R-zero states. Here we have used the Berry curvature in k -space interpretation of the spin-Chern number⁴⁶ as opposed to the original formulation in terms of twisted boundary conditions.^{57,67} We will often refer to C_σ as the spin Chern number as well, since in the case of S^z conservation—which applies to all cases considered in this work—the spin Chern number is proportional C_σ , up to a sign determined by convention. More importantly, it is the parity—even or oddness—of C_σ , not its sign, that determines the time-reversal topological \mathbb{Z}_2 index. When S^z is not a good quantum number, the expression Eq. (9) for the spin Chern number defined in the thermodynamic limit – that is without twisted boundary conditions – may be generalized to the case without S^z conservation rigorously.^{46,68} Even though we will not consider these situations in this work, we would like to point out that it is certainly possible to generalize our numerical methods for the computation of the spin Chern number and hence the \mathbb{Z}_2 index for interacting systems where S^z is not conserved.

The inversion symmetric invariant of Eq. (7) and the S^z conserving spin Chern number of Eq. (9) exhibit a complementary relationship. The former is only applicable to inversion symmetric Hamiltonians, but does not require the S^z conservation. The latter, however, does not require inversion symmetry but is nevertheless conveniently computed only for S^z conserving Hamiltonians (*e.g.* the staggered potential cases⁶⁹). Moreover, the spin Chern number, which may be any integer value in the thermodynamic limit, carries more information and thus a finer topological classification than the \mathbb{Z}_2 index, and can remain quantized even when time-reversal symmetry is broken. However there is an obvious bias towards

favoring Eq. (7) because by construction it is always integral in finite sized systems. Whilst Eq. (9) will in general yield non-integral values in finite-size systems where the Berry curvature over the BZ is no longer smooth. The practicalities of numerically computing the spin Chern number and its sensitivities to finite system size will be the subject of our next discussion.

For an interacting system, we compute the zero-frequency single-particle Green's function with QMC and then determine its eigenvectors and eigenvalues. The determination of the topological response of a system by the zero-frequency Green's function has been demonstrated in both the non-interacting and interacting limit in Ref.[41]. Both expressions (7) and (9) sidestep difficulties associated with using twisted boundary conditions,⁴³ which requires multiple numerically expensive calculations of a non-degenerate ground state. It is also inapplicable when artificial edge degeneracies⁴⁴ are encountered and is usually only practical with exact diagonalization.³⁹

The fact that both of the expressions and their interacting generalizations⁴¹ only rely on the zero-frequency single-particle Green's functions, is very convenient since more sophisticated numerical simulation methods like QMC and Dynamical Mean-field Theory⁷⁰ (which cannot provide ground state wave functions) can be implemented in determining the topological phases with interactions. The zero-frequency property also implies that numerical analytical continuation does not need to be employed. The computation of Eq. (7) for finite-size interacting systems has been previously performed in Refs. [32,33], and is straightforward. There is, however, a requirement that only cluster shapes with BZs containing a TRIM points may be studied with this method.

By contrast computing, Eq. (9) for interacting systems is a relatively new enterprise and we describe our numerical method for its computation in finite sizes in Appendix B. Our results for the non-interacting GKM model are shown in Fig. 7. It is evident that, even in the non-interacting limit, this method of evaluating the spin Chern number suffers from strong finite-size effects, though it is free of any physical effects associated with twisted boundary conditions. For small sizes, such as 6×6 and 12×12 , the resulting C_σ are not well approximated by integer values, but the discontinuous jump at the transition can still be detected by inspection. Only upon increasing the system size do the spin Chern numbers and their discontinuous jumps converge to integers. A finite size scaling analysis is needed to extrapolate to the thermodynamically limit.

The finite-size effects present in these non-interacting cases will be important for interpreting the fully interacting system that we will turn to shortly. However, the precise critical value of $t_{3N}^c = \frac{1}{3}t$ is clearly seen from the data for all system sizes to identify the topological phase transition. In particular, for the 400×400 cluster, the variation is $|\Delta C_\sigma| = 3$ across the topological phase transition. As we mentioned earlier, this is consistent with the gap closing at the $M_{1,2,3}$ points.

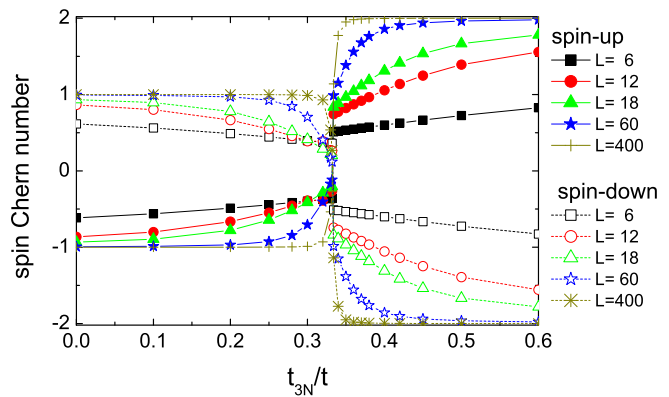


FIG. 7. (Color online) The spin Chern numbers C_σ vs t_{3N} for the non-interacting GKM model at $\lambda_{SO} = 0.4t$ for different cluster sizes. For $t_{3N} < \frac{1}{3}t$, the system is a \mathbb{Z}_2 topological insulator with $|C_\sigma| = 1$. For $t_{3N} > \frac{1}{3}t$, the system is a trivial insulator but with $|C_\sigma| = 2$.

As was alluded to earlier, the source of the “non-integerness” of the Chern number is associated with the need to approximate the k -space gradients of projector P_σ from a finite set of points in the BZ, cf Eq. (B4). This also implies that – rigorously speaking – an exact integer value is only ever attainable in the thermodynamic limit. This is an important implication since it means that topological classification as captured by the Chern number and its myriad generalization is an effect that is only rigorously stably protected in the thermodynamic limit. This is intuitively clear since, only in the thermodynamic limit do the energy gaps between smoothly connected Bloch states collapse. The remaining finite energy gaps are the *band gaps* that are the source of the topological protection of a ground state.

The finite-size computations of Eq. (9) shown in Fig. 7 with non-integral results are an honest reflection of the limitation of working with finite-size clusters. We note that an alternative method by Fukui *et. al.*⁷¹ sidesteps this with a construction which always yields an integer result. However this can be misleading since the accuracy of the results requires a critical mesh size, which Fukui *et. al.* have estimated. Moreover, the integer values obtained by their method excludes the possibility of using a finite-size scaling analysis to judge the convergence of their results and is a weakness in their method. These considerations also apply to the integral inversion \mathbb{Z}_2 invariant $(-1)^\nu$ which should and does fluctuate with cluster size: There is a shift in boundaries based on this invariant with changing cluster size and shape.

The need for large cluster sizes, however, is compensated by the QMC method which provides access to ground state correlators of cluster sizes significantly larger than those manageable by exact diagonalization. Furthermore, it is not necessary to have a manifold of ground states (which also has to be of a sufficient density) as is required with the twisted boundary conditions

method. Another important point to note from Fig. 7 is that at a fixed cluster size, the tendency to an integer value improves, the further away the tuning parameter is from the critical point. Furthermore the many-body excitation gap remains open through that portion of parameter space and the single particle Green's function at zero frequency develops no poles or singularities, permitting us to invoke the principle of adiabatic continuity and infer the thermodynamic value of the spin-Chern number of the entire portion of phase space from the finite-size scaling in the large t_{3N} limit and when $t_{3N} = 0$.

With this information the sudden discontinuity in the numerical Chern number can then be used to pinpoint the critical point. This is the general strategy that we employ in mapping out a phase diagram of both non-interacting and interacting models. In the case of an interacting model phase diagram, we have one more tuning parameter which is the interaction strength itself. The free model can then be trivially classified and when robust excitation gaps persists above the numerical ground state, the principle of adiabatic continuity can be used to reliably map out a phase diagram from sudden jumps in the numerical Chern number. As a consistency check, we also compare the spin Chern number with the \mathbb{Z}_2 invariant using Eq. (7) at various tight-binding parameters and interaction strength, as shown in Fig.8.

IV. EFFECTS OF INTERACTIONS IN HUBBARD MODEL EXTENSIONS OF THE KANE-MELE VARIANTS

We now come to the main part of the paper where we discuss the effects of the Hubbard interaction on interacting topological insulator models. To obtain ground state correlators and capture correlation effects, we use projective quantum Monte Carlo⁷²⁻⁷⁶ to study interacting variants of the KM model, Eq. (2)-(5) to which an on-site Hubbard term is added, $H \rightarrow H + \frac{U}{2} \sum_i (n_i - 1)^2$ where $U > 0$ is the strength of the repulsive on-site Hubbard interaction and n_i is the number operator on site i . In our QMC calculations, the number of sites is $N = 2 \times L^2$, where L takes the values 6, 12 and 18. The largest system sizes are far beyond current capabilities for exact diagonalization studies, rendering our “unbiased” calculations on interaction effects in topological systems important for going beyond mean-field approaches and the severe finite-size limitations of exact diagonalization studies. The QMC methodology is described in detail in Appendix A.

(i) Generalized Kane-Mele Hubbard model

We first turn our attention to interaction effects in the GKM-Hubbard model, i.e. $H_{GKM} + U$. Previously in Ref. [33], the correlation effects were discovered to result in a shift of the phase boundary that can be accurately

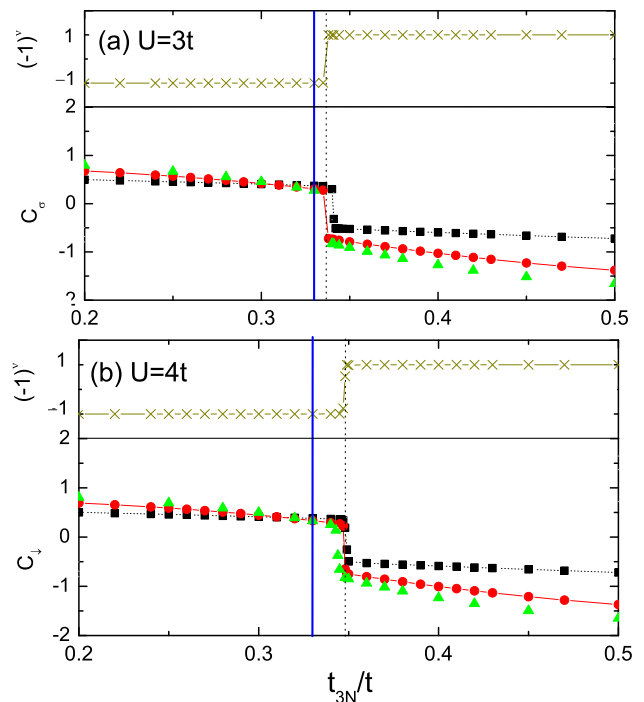


FIG. 8. (Color online) The \mathbb{Z}_2 invariant $(-1)^\nu$ (upper panels, for $L = 12$ only) and spin Chern number C_σ (lower panels) for the GKM-Hubbard model as a function of t_{3N}/t at (a) $U = 3t$ and (b) $U = 4t$. The spin-up Chern numbers C_σ are denoted by solid symbols. The spin-orbit coupling is $\lambda_{SO} = 0.4t$ and the systems sizes are chosen as 6×6 (black squares), 12×12 (red circles) and 18×18 (green triangles). $t_{3N}^c = \frac{1}{3}t$ (vertical blue line) is the critical point for the non-interacting limit.

computed with QMC simulations: with increasing U , t_{3N}^c shifts to larger values (compared to the vertical blue line in Fig.8). This behavior was identified by evaluating the \mathbb{Z}_2 invariant from exploiting the inversion symmetry of the single-particle Green's function and using Eq. (7). The QMC results³³ showed that at $U = 4t$ the topological phase transition boundary moves into the trivial insulator phase by roughly 10%. Thus, correlation *stabilizes* the topological phase in the GKM-Hubbard model.

Here we demonstrate that the topological phase transition can also be clearly identified by computing the spin Chern numbers,³⁷ as shown in the lower panels of Fig. 8. We chose intermediate interaction strengths $U = 3t$ and $U = 4t$, which are below the threshold required to induce magnetic ordering or any other symmetry breaking.³³ For comparison, we also depict the \mathbb{Z}_2 invariant vs t_{3N} for the 12×12 cluster. For both U values, Figs.8 (a) and (b) show marked changes in the spin Chern number at the same locations, as the \mathbb{Z}_2 invariant varies for the 12×12 cluster (guided by the dotted lines).

We observe that in the GKM-Hubbard model the QMC sampling still maintains the time-reversal symmetric relation $C_\uparrow = -C_\downarrow$ within tiny error bars, so long as t_{3N} is far from the phase boundary. When the value of t_{3N} is close to the topological phase transition, one needs to

increase the sampling to recover the relation. Similar to the non-interacting limit, the spin Chern numbers in Figs. 8 converge to integers only as t_{3N} is far away from the critical point. The spin-up Chern numbers in the \mathbb{Z}_2 regime is $C_\uparrow \simeq +1$ ($t_{3N} = 0.2t$) and turns to $C_\uparrow \simeq -2$ after the topological phase transitions ($t_{3N} = 0.5t$), indicated in the 12×12 and 18×18 clusters. The significant variation in C_σ , $|\Delta C_\sigma| \simeq 3$, can be used to identify the parameter-driven topological phase transition at finite U in the finite-size clusters. Moreover by adiabatic continuity to the non-interacting limit, we can also confidently identify the two phases between the topological phase transition.

Next we present the finite-size analysis for the spin Chern number in the GKM-Hubbard model, shown in Fig.9. Since only three different sizes, 6×6 , 12×12 and 18×18 are available, we are unable to fully capture the scaling behavior. However, the trends are sufficient to infer the value of the thermodynamic spin Chern number. On the other hand, the judgement can be also arrived at by the principle of adiabatic continuity to the non-interacting limit of the GKM model. We tentatively

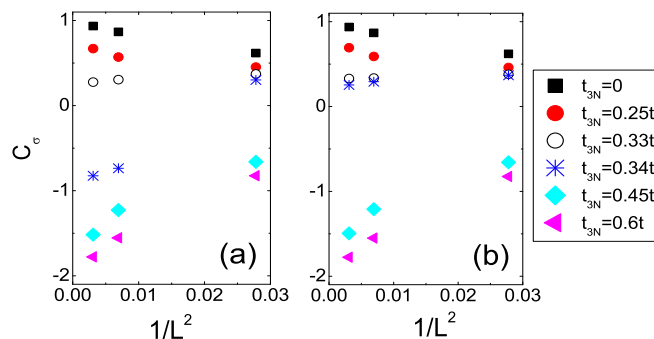


FIG. 9. (Color online) The tentative finite-size analysis of the spin-up Chern number C_\uparrow of the GKM-Hubbard model at (a) $U = 3t$ and (b) $U = 4t$ vs $1/L^2$.

consider the Chern number scaling as $1/L^2$ in Fig. 9 (or $1/L$, not shown here); showing that as the value of t_{3N} is far away from the critical point, the spin Chern numbers extrapolate well to whole integers, $C_\uparrow = 1$ or $C_\uparrow = -2$ in the thermodynamic limit. Thus, these scaling curves are still helpful in distinguishing the topological states with $C_\sigma = 1$ and $C_\sigma = -2$.

Note that near the transition (about $t_{3N} = 0.33t$ and $0.34t$), the scaling analysis is less reliable and one needs bigger sizes to determine the behavior. However, it is still helpful in determining the location of the topological phase transition. In Fig. 9 (a), we can recognize that at $t_{3N} = 0.34t$ the spin Chern number shows a drop with increasing system size; thus it is a trivial state. By contrast, Fig. 9 (b) shows that the spin Chern number at $t_{3N} = 0.34$ does not show a clear drop, suggesting that it is still in the topological insulator regime. Thus, interactions stabilize the topological phase in the GKM-Hubbard model. Note that for t_{3N} values away from

the critical value, the finite size scaling behavior is much clearer in terms of how the thermodynamic limit is approached.

Although the values of the spin Chern number suffer from strong finite-size effects, the topological phase transition boundary determined by the topological invariant in the GKM-Hubbard model has weak finite-size dependence. For $U = 3t$, on the 6×6 , 12×12 , and 18×18 clusters, $t_{3N}^c = 0.341t$, $0.337t$ and $0.335t$, respectively. For $U = 4t$, t_{3N}^c are $0.349t$, $0.347t$ and $0.345t$, respectively, suggesting the spin Chern number is a *reliable* means to detect topological phase transitions in interacting systems.

These interaction effects that cause the critical boundary in phase space to shift must originate from the dynamical quantum fluctuations, since the Hartree-Fock mean-field theory is unable to capture any phase boundary shift (for the U values we consider below the magnetic phase transition).^{33,77} We were not able to develop a perturbative argument for this shift, either.

(ii) Dimerized Kane-Mele Hubbard model

We next turn to the DKM-Hubbard model:⁴⁰ $H = H_{DKM} + U$. Recall that at $U = 0$, the critical point occurs at $t_d^c = 2t$ and is independent of value of λ_{SO} . Similar to the GKM-Hubbard model, correlation effects induce a shift of the phase boundary, but the critical value of t_d moves *towards* (into) the topological phase. In other words, correlation *destabilizes* the topological insulator phase—a behavior opposite to the GKM-Hubbard model. With finite interactions at $U = 2t$ and $\lambda_{SO} = 0.2t$, t_d^c is determined within 1.94 and 1.96 by observing the Green's function behavior and the \mathbb{Z}_2 topological invariant.⁴⁰

Here we also employ the QMC combined with the computation of the spin Chern number using Eq. (9) and the \mathbb{Z}_2 index using Eq. (7). Likewise, the values of U we considered were below the magnetic transition. Figs. 10 (a) and (b) show C_\uparrow and the \mathbb{Z}_2 index vs t_d for $U = 2t$ and $U = 4t$, respectively. In the 12×12 cluster (red circles), we can see that the spin Chern number jumps at $t_d = 1.97t$ for $U = 2t$ and $t_d = 1.76t$ for $U = 4t$, and, simultaneously, the value of the \mathbb{Z}_2 index turns from $(-1)^\nu = -1$ to 1 (guided by the dot lines). More strongly in the 12×12 cluster, one sees that the topological phase transition occurs between the $|C_\sigma| = 1$ state to the $|C_\sigma| = 0$ state and a variation $|\Delta C_\sigma| \approx 1$.

Surprisingly, compared to the GKM-Hubbard model, the interaction in the DKM model brings about a more significant shift in the location of the topological phase transition. In the $L = 12$ cluster, t_d^c at $U = 2t$ is estimated to be $1.97t - 1.98t$, whereas at $U = 4t$ it lies within $1.76t - 1.77t$. The critical point has shifted by roughly 25%. The DKM-Hubbard model also has weaker finite-size effects on the topological phase boundaries. For the $L = 6$ cluster, t_d^c s are estimated around $1.95t - 1.96t$ and $1.75t - 1.76t$ for $U = 2t$ and $4t$, respectively. The compar-

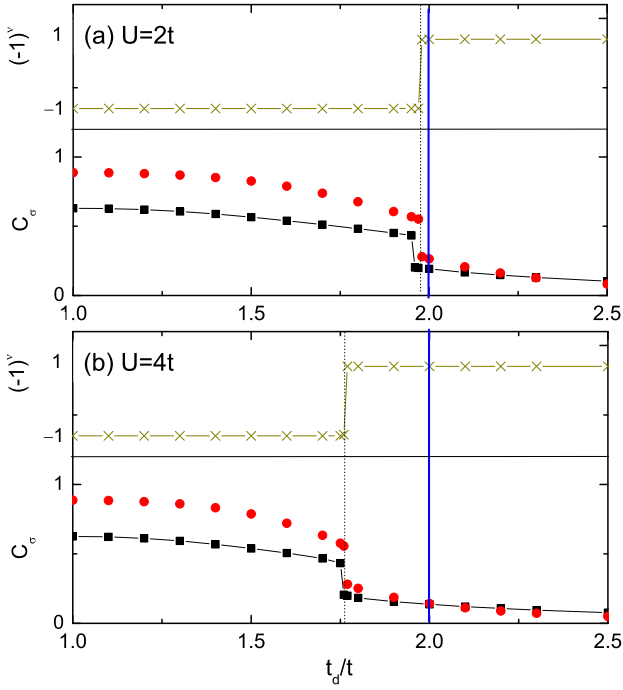


FIG. 10. (Color online) The \mathbb{Z}_2 invariant $(-1)^\nu$ (upper panels, for $L = 12$ only) and C_σ (lower panels) for the DKM-Hubbard model as a function of t_d/t at (a) $U = 2t$ and (b) $U = 4t$. $\lambda_{SO} = 0.2t$ and the systems sizes are chosen as 6×6 (black squares) and 12×12 (red circles). At $t_d = t$, the system reduces to the standard KM model and $t_d = 2t$ (vertical blue line) is the critical point for the non-interacting limit. For the sake of clarity, only the data for C_\uparrow is presented here.

ison of the results for the two cluster sizes show similar locations of the topological phase boundaries, thus suggesting weak finite-size effect on the critical points.

(iii) t_L - and t_{3N} -Dimerized Kane-Mele Hubbard models

Lastly, we present QMC results for the on-site Hubbard models of the t_L -Kane-Mele model Eq. (4) and the t_{3N} -dimerized KM model Eq. (5). These two models represent polar opposites with regard to their non-interacting hopping Hamiltonians. The former like the GKM model preserves the full D_6 point group, whilst the later breaks it down almost completely to just the inversion subgroup $\mathbb{Z}_2^{(i)}$. Thus, the t_{3N} -dimerized KM model is even less symmetric than the DKM model. The motivation for considering these other variants is to demonstrate more examples of interacting TI phases and the role crystal symmetry or lack thereof might play and help contrast the different outcomes of explicitly breaking or preserving the crystal symmetry of the underlying KM model. Given that for the hopping Hamiltonians that we have set out to study, the crystal symmetry already greatly influences the low-energy character of the critical

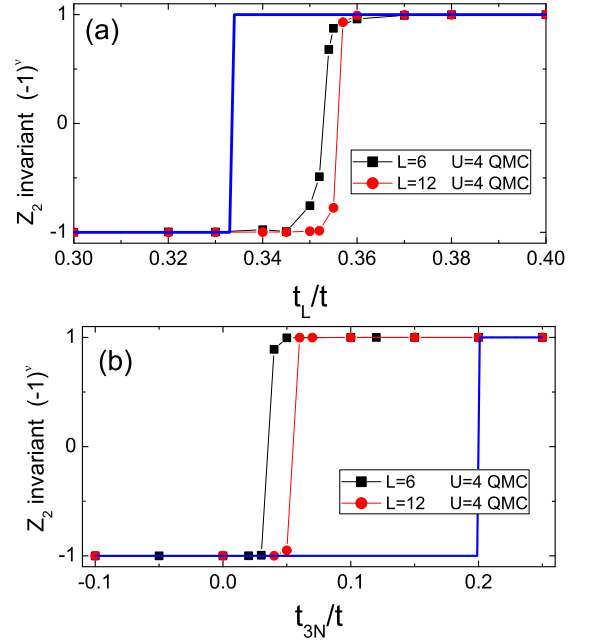


FIG. 11. (Color online) The \mathbb{Z}_2 invariants for interacting and noninteracting cases in the (a) t_L -KM model and (b) t_{3N} -dimerized KM model at $t_d = 1.8t$. For reference purposes, the non-interacting \mathbb{Z}_2 invariant were computed and presented as the blue lines using $L \times L = 1200 \times 1200$ clusters. The symbols depict the interacting \mathbb{Z}_2 invariant by the QMC for $U = 4t$ on 6×6 (black squares) and 12×12 (red circles). All calculations are performed with $\lambda_{SO} = 0.4t$.

theory – such as deciding the number of Dirac cones – between the topological insulator phase and the normal insulator phase, it is reasonable to expect that crystal symmetry will have a significant role to play in shifting phase boundaries.

The QMC results of the correlation effects on these two models are displayed in Fig. 11 where we still used $\lambda_{SO} = 0.4t$ and $U = 4$ to compare with Fig. 8 and Fig. 10. For simplicity, we only show the \mathbb{Z}_2 invariants as a function of the tight-binding parameters: t_L and t_{3N} in Eq. (4) and Eq. (5), respectively. Note that, near the critical point, $(-1)^\nu$ shows a poor approximation to an integer value (not $\simeq 1$ or $\simeq -1$), meaning that more QMC samplings are required. However, we still can distinguish the locations of the correlated topological phase boundaries. From Fig. 11 (a), it is clear that with finite interaction, the topological phase transition shifts towards (into) to the trivial insulator regime; the topological phase is enlarged and thus correlation *stabilizes* the topological insulator state in the t_L -KM model. For the 6×6 cluster, $t_L^c = 0.352t - 0.354t$, and for the 12×12 cluster, $t_L^c = 0.352t - 0.355t$. Like the GKM model, the t_L^c has weak finite-size effect on the phase boundaries.

In the next panel, Fig. 11 (b) exhibits the interacting \mathbb{Z}_2 invariant against the t_{3N} parameter for the t_{3N} -dimerized KM model at $t_d = 1.8t$. The non-interacting limit, $t_{3N}^c = 0.2t$, is indicated by the blue line. Turning

on interaction, the phase boundary moves towards (into) the topological state regime; thus correlation *destabilizes* the topological insulator phase. We have numerically examined that with finite bond dimerization, the topological critical points are always pushed to the topological insulator regime under correlation.

Our observations of the effects of Hubbard-type interactions on these KM model variants show a systematic pattern: The stability of the topological insulator phase as measured by its occupied volume in the phase diagram is diminished when more of the symmetries of the D_6 point group of the lattice are explicitly broken by the Hamiltonian. A posteriori, we elevate our observations to a speculative conjecture of a principle: in the absence of any spontaneous symmetry breaking, the Hubbard interaction will displace the critical line of the interacting topological quantum phase transition in favor of the normal insulator phase if fewer crystal point group symmetries – but which must include inversion – are present in the non-interacting portion of the tight-binding Hamiltonian. The condition regarding spontaneous symmetry breaking excludes competition with magnetic and density-waves phases. This is important to state since at very strong coupling either phase gives way to the Néel ordered phase. It is worth reiterating that due to the special form of these Hamiltonians at half-filling, the QMC methodology employed is free of sign-problems and is essentially an exact method for finite clusters up to statistical noise; which can always be systematically improved with greater sampling. In a related study⁷⁸ of the plaquette KM model, which is not too dissimilar from the ones we have considered, qualitatively consistent results are obtained.

V. DISCUSSIONS

We make a few remarks regarding low energy effective theories and present some related speculations. As was previously mentioned, mean-field calculations at the level of the Hartree-Fock approximation in the KM model⁷⁷ and also our own computations³³ for models Eqs. (2)-(5) are unable to demonstrate a continuous shift in the topological quantum phase transition boundaries at weak coupling, although a transition to a magnetic state does occur at strong coupling. We rationalize this by noting that the Hubbard U in *two dimensions* for a low energy effective critical field theory of gapless linearly dispersing Dirac fermions is *irrelevant* under scaling. In fact, as is well known⁷⁹ even in the case of long-range Coulomb interactions in graphene, which is a archetype for this variety of field theory, a Renormalization Group (RG) analysis also produces the conclusion that the Dirac nodes are perturbatively stable, albeit with anomalous scaling dimensions due to quantum fluctuations. Thus the phase boundary shifts – significantly observable only at relatively large $U \sim 3t$ – that we have observed in our QMC exact computations are effects at intermediately

strong interactions, which is beyond the weak-coupling low energy-effective theory description. The implications are that the standard field theoretic RG computations at one loop order would be unreliable in capturing the intermediately strong coupling physics of interest.

Nevertheless, we speculate that an explanation of the dichotomous behavior of the phase boundary shifts must involve the fact that there are a different number of Dirac cones present at the critical topological transition point (*three* in the GKM and t_L -KM models but *one* in the DKM and t_{3N} -dimerized KM models) and that this is the main influence of point group symmetry to the low energy physics. It is tempting to relate our observations to a large- N study⁸⁰ of graphene with Hubbard interactions, but we are cautious and reluctant to since $N = 1, 3$ is a very small value of N . In spite of this, Functional Renormalization Group (fRG)⁸¹ computations or more recent dimensional regularization $d = 3 - \epsilon, \epsilon = 1$ studies^{82,83} applied to the Hubbard graphene system have been encouraging in describing physics near strong coupling. We will leave these very interesting lines of investigations for future work, as these computations are by no means trivial undertakings.

VI. SUMMARY AND CONCLUSIONS

In this work we have analyzed variants of the archetypical model of a time-reversal symmetric topological insulator, the Kane-Mele model. These generalized models Eqs. (2)-(5) exhibit various space group symmetries of the honeycomb lattice on which they are formulated. In the non-interacting limit, all of the models exhibit a topological phase transitions between a \mathbb{Z}_2 topological insulator phase and a normal insulating phase. By means of the unbiased QMC method, we further study the interacting variants of these model systems by including on-site Hubbard interactions. The projective determinant QMC method that we employ is free of sign problems (at half-filling which is the only filling considered) and is essentially exact up to statistical sampling noise. The regime that interests us most is the intermediately strong U regime before magnetic order sets in. We demonstrate that the topological phase of our numerically exact interacting ground states can be ascertained by computing either the \mathbb{Z}_2 invariant or the spin Chern number C_σ via the zero-frequency single-particle Green's function. Thus our work is a numerical implementation of the theoretical proposal of Refs. [41 and 42] for finite-size clusters using reliably accurate QMC. The spin Chern number had not been previously computed with QMC, and we argue on technical grounds that it is complementary to the inversion symmetry based expression for the \mathbb{Z}_2 invariant.

Accompanied with finite-size scaling analyses and adiabatic continuity to non-interacting limits, – which we numerically observe – we argue that the spin Chern number is a robust classification method of interacting TI's. Moreover the spin Chern number may be utilized in cir-

cumstances where inversion and even time-reversal symmetry are absent, and may be generalized to the case where S^z conservation is absent.⁴⁶ Our numerically exact QMC results suggest that quantum fluctuations from intermediately strong interactions can act to either stabilize or destabilize the topological phase, depending on whether the hopping terms preserve or break lattice symmetries (when U is less than the value which induces magnetism). Although admittedly bold and speculative, we conjecture a principle that in the situations where spontaneous symmetry breaking phases are excluded, on-site Hubbard interactions will destabilize the TI phase in honeycomb models when the lattice point group D_6 is explicitly broken down to a subgroup containing $\mathbb{Z}_2^{(i)}$ inversion by the tight-binding Hamiltonian, and stabilized when the full D_6 symmetry is preserved. We speculate that the mechanism by which this acts is through influ-

encing the form of low energy theory at the quantum critical point – which needs to be handled beyond perturbatively weak coupling – and suggest further avenues of investigation. We hope our work will help stimulate further studies in this direction and provide a baseline for the general expectations for unbiased calculations of correlation effects on topological phase transitions.

We are grateful for discussions with Q. Niu, D. N. Sheng, K. Sun, C. Varney, Z. Wang, S. Yang, W-C Lee. This work was supported by ARO Grant No. W911NF-09-1-0527, NSF Grant No. DMR-0955778, and by grant W911NF-12-1-0573 from the Army Research Office with funding from the DARPA OLE Program. Simulations were run on the Texas Advanced Computing Center (TACC) at the University of Texas at Austin, <http://www.tacc.utexas.edu>, and the Brutus cluster at ETH Zurich. VC gratefully acknowledges the support from the DOE grant DE-FG02-07ER46453.

-
- ¹ M. W. Young, S.-S. Lee, and C. Kallin, *Phys. Rev. B* **78**, 125316 (2008).
² D. Pesin and L. Balents, *Nat. Phys.* **6**, 376 (2010).
³ M. Kargarian and G. A. Fiete, *Phys. Rev. B* **82**, 085106 (2010).
⁴ R. Li, J. Wang, X.-L. Qi, and S.-C. Zhang, *Nat. Phys.* **6**, 284 (2010).
⁵ M. Hohenadler, T. C. Lang, and F. F. Assaad, *Phys. Rev. Lett.* **106**, 100403 (2011).
⁶ M. Hohenadler, Z. Y. Meng, T. C. Lang, S. Wessel, A. Muramatsu, and F. F. Assaad, *Phys. Rev. B* **85**, 115132 (2012).
⁷ D. Zheng, G.-M. Zhang, and C. Wu, *Phys. Rev. B* **84**, 205121 (2011).
⁸ B. Swingle, M. Barkeshli, J. McGreevy, and T. Senthil, *Phys. Rev. B* **83**, 195139 (2011).
⁹ J. Maciejko, X.-L. Qi, A. Karch, and S.-C. Zhang, *Phys. Rev. Lett.* **105**, 246809 (2010).
¹⁰ M. Kargarian and G. A. Fiete, *Phys. Rev. Lett.* **110**, 156403 (2013).
¹¹ M. Levin and A. Stern, *Phys. Rev. B* **86**, 115131 (2012).
¹² M. Levin and A. Stern, *Phys. Rev. Lett.* **103**, 196803 (2009).
¹³ J. E. Moore, Y. Ran, and X.-G. Wen, *Phys. Rev. Lett.* **101**, 186805 (2008).
¹⁴ T. Neupert, L. Santos, S. Ryu, C. Chamon, and C. Mudry, *Phys. Rev. B* **84**, 165107 (2011).
¹⁵ A. Rüegg and G. A. Fiete, *Phys. Rev. Lett.* **108**, 046401 (2012).
¹⁶ X. Wan, A. M. Turner, A. Vishwanath, and S. Y. Savrasov, *Phys. Rev. B* **83**, 205101 (2011).
¹⁷ M. Hohenadler and F. F. Assaad, *J. Phys. Cond. Matt.* **25**, 143201 (2013).
¹⁸ G. A. Fiete, V. Chua, M. Kargarian, R. Lundgren, A. Rüegg, J. Wen, and V. Zyuzin, *Physica E* **44**, 845 (2012).
¹⁹ J. Maciejko, V. Chua, and G. A. Fiete, *Phys. Rev. Lett.* **112**, 016404 (2014).
²⁰ J. Maciejko and A. Rüegg, *Phys. Rev. B* **88**, 241101 (2013).
²¹ J. E. Moore, *Nature* **464**, 194 (2010).
²² M. Z. Hasan and C. L. Kane, *Rev. Mod. Phys.* **82**, 3045 (2010).
²³ X.-L. Qi and S.-C. Zhang, *Rev. Mod. Phys.* **83**, 1057 (2011).
²⁴ M. König, S. Wiedmann, C. Brune, A. Roth, H. Buhmann, L. Molenkamp, X.-L. Qi, and S.-C. Zhang, *Science* **318**, 766 (2007).
²⁵ A. Roth, C. Brüne, H. Buhmann, L. W. Molenkamp, J. Maciejko, X.-L. Qi, and S.-C. Zhang, *Science* **325**, 294 (2009).
²⁶ D. Hsieh, D. Qian, L. Wray, Y. Xia, Y. Hor, R. J. Cava, and M. Z. Hasan, *Nature* **452**, 970 (2008).
²⁷ S. Raghu, X.-L. Qi, C. Honerkamp, and S.-C. Zhang, *Phys. Rev. Lett.* **100**, 156401 (2008).
²⁸ Y. Zhang, Y. Ran, and A. Vishwanath, *Phys. Rev. B* **79**, 245331 (2009).
²⁹ J. Wen, A. Rüegg, C.-C. J. Wang, and G. A. Fiete, *Phys. Rev. B* **82**, 075125 (2010).
³⁰ Q. Liu, H. Yao, and T. Ma, *Phys. Rev. B* **82**, 045102 (2010).
³¹ A. Rüegg and G. A. Fiete, *Phys. Rev. B* **84**, 201103 (2011).
³² A. Go, W. Witczak-Krempa, G. S. Jeon, K. Park, and Y. B. Kim, *Phys. Rev. Lett.* **109**, 066401 (2012).
³³ H.-H. Hung, L. Wang, Z.-C. Gu, and G. A. Fiete, *Phys. Rev. B* **87**, 121113 (2013).
³⁴ J. C. Budich, R. Thomale, G. Li, M. Laubach, and S.-C. Zhang, *Phys. Rev. B* **86**, 201407 (2012).
³⁵ J. C. Budich, B. Trauzettel, and G. Sangiovanni, *Phys. Rev. B* **87**, 235104 (2013).
³⁶ L. Wang, X. Dai, and X. C. Xie, *Euro. Phys. Lett.* **98**, 57001 (2012).
³⁷ T. Yoshida, R. Peters, S. Fujimoto, and N. Kawakami, *Phys. Rev. B* **87**, 085134 (2013).
³⁸ C. N. Varney, K. Sun, M. Rigol, and V. Galitski, *Phys. Rev. B* **82**, 115125 (2010).
³⁹ C. N. Varney, K. Sun, M. Rigol, and V. Galitski, *Phys. Rev. B* **84**, 241105 (2011).
⁴⁰ T. C. Lang, A. M. Essin, V. Gurarie, and S. Wessel, *Phys.*

- Rev. B **87**, 205101 (2013).
- ⁴¹ Z. Wang and S.-C. Zhang, Phys. Rev. X **2**, 031008 (2012).
- ⁴² Z. Wang, X.-L. Qi, and S.-C. Zhang, Phys. Rev. B **85**, 165126 (2012).
- ⁴³ Q. Niu, D. J. Thouless, and Y.-S. Wu, Phys. Rev. B **31**, 3372 (1985).
- ⁴⁴ T. Fukui and Y. Hatsugai, Phys. Rev. B **75**, 121403 (2007).
- ⁴⁵ L. Fu and C. L. Kane, Phys. Rev. B **76**, 045302 (2007).
- ⁴⁶ E. Prodan, Phys. Rev. B **80**, 125327 (2009).
- ⁴⁷ C. L. Kane and E. J. Mele, Phys. Rev. Lett. **95**, 226801 (2005).
- ⁴⁸ C. L. Kane and E. J. Mele, Phys. Rev. Lett. **95**, 146802 (2005).
- ⁴⁹ B. A. Bernevig, T. L. Hughes, and S.-C. Zhang, Science **314**, 1757 (2006).
- ⁵⁰ A. P. Schnyder, S. Ryu, A. Furusaki, and A. W. Ludwig, in *American Institute of Physics Conference Series*, Vol. 1134 (2009) pp. 10–21.
- ⁵¹ A. Kitaev, in *ADVANCES IN THEORETICAL PHYSICS: Landau Memorial Conference*, Vol. 1134 (AIP Publishing, 2009) pp. 22–30.
- ⁵² X.-L. Qi, T. L. Hughes, and S.-C. Zhang, Phys. Rev. B **78**, 195424 (2008).
- ⁵³ L. Fu, C. L. Kane, and E. J. Mele, Phys. Rev. Lett. **98**, 106803 (2007).
- ⁵⁴ J. E. Moore and L. Balents, Phys. Rev. B **75**, 121306 (2007).
- ⁵⁵ We have also specialized to the case where there is also only a single valence and conduction band per-spin species.
- ⁵⁶ D. N. Sheng, Z. Y. Weng, L. Sheng, and F. D. M. Haldane, Phys. Rev. Lett. **97**, 036808 (2006).
- ⁵⁷ L. Sheng, D. N. Sheng, C. S. Ting, and F. D. M. Haldane, Phys. Rev. Lett. **95**, 136602 (2005).
- ⁵⁸ M. A. N. Araújo, E. V. Castro, and P. D. Sacramento, Phys. Rev. B **87**, 085109 (2013).
- ⁵⁹ Y. Hatsugai, M. Kohmoto, and Y.-S. Wu, Phys. Rev. B **54**, 4898 (1996).
- ⁶⁰ C. Xu and J. E. Moore, Phys. Rev. B **73**, 045322 (2006).
- ⁶¹ See the supplemental material in Ref. [33].
- ⁶² V. Gurarie, Phys. Rev. B **83**, 085426 (2011).
- ⁶³ S. R. Manmana, A. M. Essin, R. M. Noack, and V. Gurarie, Physical Review B **86**, 205119 (2012).
- ⁶⁴ Y. You, Z. Wang, J. Oon, and C. Xu, ArXiv e-prints (2014), arXiv:1403.4938 [cond-mat.str-el].
- ⁶⁵ W. Brinkman and T. Rice, Physical Review B **2**, 4302 (1970).
- ⁶⁶ J. E. Avron, R. Seiler, and B. Simon, Phys. Rev. Lett. **51**, 51 (1983).
- ⁶⁷ D. N. Sheng, L. Balents, and Z. Wang, Phys. Rev. Lett. **91**, 116802 (2003).
- ⁶⁸ E. Prodan, New J. Phys. **12**, 065003 (2010).
- ⁶⁹ H.-H. Lai and H.-H. Hung, Phys. Rev. B **89**, 165135 (2014).
- ⁷⁰ A. Georges, G. Kotliar, W. Krauth, and M. J. Rozenberg, Rev. Mod. Phys. **68**, 13 (1996).
- ⁷¹ T. Fukui, Y. Hatsugai, and H. Suzuki, J. Phys. Soc. Jpn. **74**, 1674 (2005).
- ⁷² G. Sugiyama and S. E. Koonin, Ann. Phys. **168**, 1 (1986).
- ⁷³ S. Sorella, S. Baroni, R. Car, and M. Parrinello, Europhys. Lett. **8**, 663 (1989).
- ⁷⁴ S. R. White, D. J. Scalapino, R. L. Sugar, E. Y. Loh, J. E. Gubernatis, and R. T. Scalettar, Phys. Rev. B **40**, 506 (1989).
- ⁷⁵ F. F. Assaad, *Quantum Monte Carlo methods on lattices: The determinantal approach in Quantum Simulations of Complex Many-Body Systems: From Theory to Algorithms, Lecture Notes* (NIC Series Vol. **10**, 2002).
- ⁷⁶ F. F. Assaad, AIP Conf. Proc. **678**, 117 (2003).
- ⁷⁷ S. Rachel and K. Le Hur, Phys. Rev. B **82**, 075106 (2010).
- ⁷⁸ W. Wu, S. Rachel, W.-M. Liu, and K. Le Hur, Phys. Rev. B **85**, 205102 (2012).
- ⁷⁹ J. González, F. Guinea, and M. Vozmediano, Nuclear Physics B **424**, 595 (1994).
- ⁸⁰ I. F. Herbut, Physical review letters **97**, 146401 (2006).
- ⁸¹ L. Janssen and I. F. Herbut, ArXiv e-prints (2014), arXiv:1402.6277 [cond-mat.str-el].
- ⁸² I. F. Herbut, V. Juričić, and O. Vafek, Physical Review B **80**, 075432 (2009).
- ⁸³ F. F. Assaad and I. F. Herbut, Physical Review X **3**, 031010 (2013).
- ⁸⁴ Z. Y. Meng, T. C. Lang, S. Wessel, F. F. Assaad, and A. Muramatsu, Nature **464**, 847 (2010).
- ⁸⁵ H.-H. Hung, *Exotic quantum magnetism and superfluidity in optical lattices* (PhD thesis, University of California, San Diego, 2011).
- ⁸⁶ N. Metropolis, A. W. Rosenbluth, M. N. Rosenbluth, A. H. Teller, and E. Teller, J. Chem. Phys. **21**, 1087 (1953).
- ⁸⁷ J. E. Hirsch, Phys. Rev. B **31**, 4403 (1985).
- ⁸⁸ F. F. Assaad and M. Imada, J. Phys. Soc. Jpn. **65**, 189 (1996).

Appendix A: Quantum Monte Carlo

The projective quantum Monte Carlo method (QMC) is given by projecting an arbitrary trivial wave function $|\psi_T\rangle$ (requiring $\langle\psi_T|\psi_0\rangle \neq 0$) onto the ground state wave function $|\psi_0\rangle$.^{72–76,84,85} The expectation value of an observable A is obtained by

$$\langle A \rangle = \lim_{\Theta \rightarrow \infty} \frac{\langle \psi_T | e^{-\frac{\Theta}{2}H} A e^{-\frac{\Theta}{2}H} | \psi_T \rangle}{\langle \psi_T | e^{-\Theta H} | \psi_T \rangle}, \quad (\text{A1})$$

where Θ is the projective parameter. To carry out the procedures numerically, we need to discretize the projection operator $e^{-\Theta H}$ into tiny time propagators $e^{-\Delta\tau H}$ with $\Theta = \Delta\tau M$: $e^{-\Theta H} = (e^{-\Delta\tau H})^M$ where M is the number of time slices and $\Delta\tau$ is chosen as a small number. The first-order Suzuki-Trotter decomposition can further decompose $e^{-\Delta\tau H}$ as

$$e^{-\Delta\tau H} \simeq e^{-\Delta\tau H_0} e^{-\Delta\tau H_U}, \quad (\text{A2})$$

where H_0 is the tight-binding Hamiltonian, which could be equation (2) and equation (3), for the GKM model and the DKM model, respectively; $H_U = \frac{U}{2} \sum_i (n_i - 1)^2$ is the repulsive Hubbard on-site interaction; $n_i = \sum_{\sigma} c_{i,\sigma}^{\dagger} c_{i,\sigma}$. To represent $e^{-\Delta\tau H_U}$ in terms of the single-particle basis, we need to implement the $SU(2)$ -invariant Hubbard-Stratonovich transformation⁸⁴

$$e^{-\Delta\tau \frac{U}{2} (n_i - 1)^2} = \frac{1}{4} \sum_{l=\pm 1, \pm 2} \gamma(l) e^{i\sqrt{\Delta\tau \frac{U}{2}} \eta(l)(n_i - 1)} + O(\Delta\tau^4)$$

where $\gamma(\pm 1) = 1 + \sqrt{6}/3$, $\gamma(\pm 2) = 1 - \sqrt{6}/3$; $\eta(\pm 1) = \pm\sqrt{2(3 - \sqrt{6})}$ and $\eta(\pm 2) = \pm\sqrt{2(3 + \sqrt{6})}$ are 4-component auxiliary fields. In the current literature, $\Delta\tau t = 0.05$ and $\Theta t = 40$ are used through the content.

Implementing equation (A2) and (A3), H turns out to be τ -dependent since H_U is associated with the auxiliary field configuration $\eta(l_{i,\tau})$; then $e^{-\Theta H} = \prod_{\tau=1}^M e^{-\Delta\tau H_\tau}$. The denominator of equation (A1) (named the projector partition function),⁷³ is evaluated as follows^{6,7,75}

$$\begin{aligned} \langle \psi_T | e^{-\Theta H} | \psi_T \rangle &= \langle \psi_T | \prod_{\tau=1}^M e^{-\Delta\tau H_\tau} | \psi_T \rangle \cong \langle \psi_T | \prod_{\tau=1}^M e^{-\Delta\tau H_0} e^{-\Delta\tau H_{U,\tau}} | \psi_T \rangle \\ &= \left(\frac{1}{4}\right)^{MN} \sum_{\{l_{i,\tau}\}} \left\{ \left(\prod_{i,\tau} \gamma(l_{i,\tau}) \right) \prod_{\sigma} \text{Tr} \left(\prod_{\tau=1}^M e^{-\Delta\tau \sum_{i,j} c_{i,\sigma}^\dagger [\mathbf{H}_0^\sigma]_{ij} c_{j,\sigma}} e^{i\sqrt{\Delta\tau} \frac{U}{2} \eta(l_{i,\tau}) (n_{i,\sigma} - \frac{1}{2})} \right) \right\} \\ &= \left(\frac{1}{4}\right)^{MN} \sum_{\{l_{i,\tau}\}} \left\{ \left(\prod_{i,\tau} \gamma(l_{i,\tau}) \right) \det \left(O_\uparrow[l_{i,\tau}] \right) \det \left(O_\downarrow[l_{i,\tau}] \right) \right\}, \end{aligned} \quad (\text{A4})$$

where $\sum_{l_{i,\tau}}$ runs over possible auxiliary configurations $\eta(l_{i,\tau})$, where $i = 1 \sim N$ are site indices and $\tau = 1 \sim M$ are imaginary time indices; \mathbf{H}_0^σ is the matrix kernel of H_0 with spin σ . Each time propagator $e^{-\Delta\tau H_0} e^{-\Delta\tau H_U}$ is a $N \times N$ matrix and $\text{Tr}(\prod_{\tau} e^{\dots}) = \det(O_\sigma)$ represents the trace over fermion degrees of freedom.

Given such a N -site and M -time slice system, the summation in the above equation has a degree of 4^{NM} , and generally, it is impossible to consider all configurations. The auxiliary field configuration, $\{\dots \eta(l_{i,\tau}) \dots\}$, however, can be determined by Monte Carlo importance samplings.^{75,76,85} For simplicity, we used the Metropolis algorithm in this paper.⁸⁶ The physical meaning of $\left(\prod_{i,\tau} \gamma(l_{i,\tau}) \right) \prod_{\sigma=\uparrow,\downarrow} \det \left(O_\sigma[l_{i,\tau}] \right)$ is the probability weight at the given auxiliary field configuration $\{\eta(l_{i,\tau})\}$.⁸⁷ When this term is proven positive-definitive, QMC simulations are free-sign and the results are numerically exact. This is always true in the half-filling Kane-Mele-type model without Rashba spin-orbital coupling.^{6,7,33,40}

To obtain zero-frequency Green's function, we first evaluate the time-displaced Green's function $G(\mathbf{r}, \tau)$. The unequal-time Green's function is defined as⁸⁸

$$\begin{aligned} G_\sigma(\tau, r_i, r_j) &= \langle \psi_0 | c_\sigma(\tau, r_i) c_\sigma^\dagger(r_j) | \psi_0 \rangle \\ &= \langle \psi_0 | e^{\tau H} c_\sigma(r_i) e^{-\tau H} c_\sigma^\dagger(r_j) | \psi_0 \rangle. \end{aligned} \quad (\text{A5})$$

Then we perform the Fourier transform from real space to momentum space $\mathbf{r} \rightarrow \mathbf{k}$, and imaginary time to the Matsubara frequency $\tau \rightarrow i\omega$,

$$G_\sigma(i\omega, \mathbf{k}) = \frac{1}{\beta} \int_0^\beta d\tau e^{i\omega\tau} \frac{1}{N} \sum_{r_i, r_j} e^{i\mathbf{k}\cdot(r_i - r_j)} G_\sigma(\tau, r_i, r_j).$$

The zero-frequency is given setting $i\omega = 0$. To calculate the spin Chern number C_σ , however, we need the single-particle Green's functions for all momentum points and implement equation (9). This procedure is slightly different from the approach to evaluate the \mathbb{Z}_2 index, for

which only time-reversal invariant momentum points are required.⁴¹ For sign-free QMC simulations, one can accurately calculate the zero-frequency Green's functions in system sizes which are larger than the small clusters in an exact diagonalization and then evaluate the spin Chern numbers using the projection operators equation (9). This approach is useful to identify different topological phases in the interacting level without using twisted boundary conditions.

Note that for more generic cases, the Green's functions are a 4×4 matrix⁵⁶, i.e.,

$$\mathbf{G} = \begin{pmatrix} G_{\uparrow\uparrow} & G_{\uparrow\downarrow} \\ G_{\downarrow\uparrow} & G_{\downarrow\downarrow} \end{pmatrix}, \quad (\text{A6})$$

where $G_{\uparrow\uparrow} = G_\uparrow$ ($G_{\downarrow\downarrow} = G_\downarrow$) as defined in equation (A5), and $G_{\uparrow\downarrow} = \langle c_\uparrow(\tau) c_\downarrow^\dagger \rangle$. Without Rashba spin-orbital coupling, however, the $G_{\sigma\sigma'} = 0$ for $\sigma \neq \sigma'$. Therefore, for the simplified Kane-Mele-type model, the Green's functions reduce to 2×2 matrix for each spin. In the main text, we implement the QMC and projection operator procedures equation (9) on the GKM and DKM model to study the parameter-induced topological phase transition.

In the noninteracting KM models, due to the inversion symmetry, the 2×2 Green's functions at the time-reversal invariant momentum points (TRIM) can be simply expressed as

$$G_{\uparrow\uparrow}(i\omega = 0, \mathbf{k}_i) = \alpha_{\mathbf{k}_i} \sigma^x, \quad \mathbf{k}_i \in \text{TRIM}, \quad (\text{A7})$$

where some coefficients multiply the σ^x Pauli matrix, and in equation (7), $\tilde{\eta}(\mathbf{k}_i) = \pm 1$ is well-defined. In the cases of finite U , $\tilde{\eta}(\mathbf{k}_i) = \pm 1$ and the relation equation (A7) are not guaranteed in a single measurement in the QMC simulations, however. Instead, they should be obtained by sufficiently large number of QMC simulations.

To interpret this, we present two benchmark results for the matrix elements of the zero-frequency Green's functions at $\mathbf{k}_i = M_1$, $g_{ij} = [G(i\omega = 0, \mathbf{M}_1)]_{ij}$, vs the number

of measurements (m) in Figs. 12. $\lambda_{SO} = 0.4t$ and $U = 4t$ are used. The test system size is 2×6^2 . To recover equation (A7), one should expect that $\text{Re}[g_{12}] \simeq \text{Re}[g_{21}]$, and $\text{Im}[g_{12}] = \text{Im}[g_{21}] = \|g_{11(22)}\| \simeq 0$. It has been demonstrated that the values of $\text{Re}[g_{12}] = \alpha_{\mathbf{k}_i}$ can be used to identify the topological property³³.

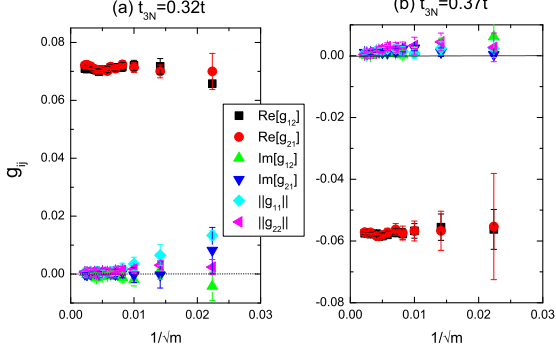


FIG. 12. (Color online) The matrix elements of the zero-frequency Green's functions $G(0, \mathbf{M}_1)$ vs the number of samplings m at (a) $t_{3N} = 0.32t$ and (b) $t_{3N} = 0.37t$. $\lambda_{SO} = 0.4t$ and $U = 4t$. $\text{Re}[g_{ij}]$ and $\text{Im}[g_{ij}]$ denote the real part and imaginary part of $[G(0, \mathbf{M}_1)]_{ij}$, respectively; $\|g_{ii}\|$ denotes the diagonal component of $G(0, \mathbf{M}_1)$ in magnitudes.

Fig. 12 (a) shows $t_{3N} = 0.32t$ in the \mathbb{Z}_2 topological insulator phase and (b) for $t_{3N} = 0.37t$ in the trivial insulator. At small m , the real parts of g_{12} and g_{21} are not equal; furthermore, g_{12} and g_{21} have imaginary parts, and both of g_{11} and g_{22} are finite. However, one can see that, upon sampling sufficient times, $\text{Re}[g_{12}] \simeq \text{Re}[g_{21}]$, and meanwhile $\text{Im}[g_{12}]$, $\text{Im}[g_{21}]$, $\|g_{11(22)}\|$ go to zero. Thus, in the $m \rightarrow \infty$ limit, equation (A7) is recovered, and then the value of $\langle \tilde{\eta}(\mathbf{k}_i) \rangle$ over QMC simulations monotonically approaches to ± 1 .

For other \mathbf{k}_i and interacting case, equation (A7) does not hold. However, for the non-interacting case we found that the value of resulting spin Chern number C_σ is not sensitive to the number of samplings provided they are large enough in number. Throughout our paper, we choose the number of measurements large enough (mostly over several thousands) to determine the 2×2 single-particle Green's function, and then calculate the spin Chern numbers.

Appendix B: Projection operator expression of the Spin-Chern number

In this section we provide a description of the projection operator expression used to evaluate the spin Chern number for finite lattices and its practical numerical implementation. The expression for the Chern numbers us-

ing the projection operators onto the occupied bands is,⁶⁶

$$\begin{aligned} C_\sigma &= \frac{1}{2\pi i} \int_{\text{B.Z.}} \text{Tr} (P_\sigma dP_\sigma \wedge dP_\sigma) \\ &= \frac{1}{2\pi i} \int_{\text{B.Z.}} \text{Tr} \left\{ P_\sigma(\mathbf{k}) \left[\partial_{k_x} P_\sigma(\mathbf{k}) \partial_{k_y} P_\sigma(\mathbf{k}) \right. \right. \\ &\quad \left. \left. - \partial_{k_y} P_\sigma(\mathbf{k}) \partial_{k_x} P_\sigma(\mathbf{k}) \right] \right\} dk_x dk_y, \end{aligned} \quad (\text{B1})$$

where $P_\sigma(\mathbf{k})$ is the spectral projector operator constructed using the Bloch eigenvectors (eigenspace) at \mathbf{k} with energies below the Fermi energy ϵ_F , i.e., $E_n(\mathbf{k}) < \epsilon_F$ and for spin sector- σ . A merit of this formulation of the Chern number is the manifest independence of the $U(1)$ phases of the Bloch states. The Bloch eigenstates themselves are obtained from diagonalizing the interacting zero-frequency Green's functions

$$G_\sigma(\mathbf{k}, 0) |\mu_i\rangle = \mu_i |\mu_i\rangle, \quad (\text{B2})$$

and then

$$P_\sigma(\mathbf{k}) = \sum_{\mu_i > 0} |\mu_i\rangle \langle \mu_i|, \quad (\text{B3})$$

where choosing $\mu_i > 0$ corresponds to selecting occupied bands $E_n < \epsilon_F$, i.e. R-zero of the $G_\sigma(\mathbf{k}, 0)$. The projection operator formula above is manifestly $U(1)$ gauge invariant. The integral is over the Brillouin zone (BZ), and, in practical numerical application, the region of integration over the BZ does not need to be a Wigner-Seitz unit cell in reciprocal lattice space, as long as the entire reciprocal lattice unit cell is covered.

In a finite-size system, the set of \mathbf{k} -vectors is discretized, so we will need to replace the integral with the summation over finite momentum points. For convenience we can map the momentum points as a $N = L_x \times L_y$ square grid of spacing h and label each \mathbf{k} with discrete coordinate indices $\{m, n\}$. Then we can approximate the partial derivatives $\partial_{k_x} P_\sigma(\mathbf{k})$ and $\partial_{k_y} P_\sigma(\mathbf{k})$ using the symmetric finite difference as

$$\begin{aligned} \partial_{k_x} P_\sigma(\mathbf{k}) &\approx \frac{P_{\sigma, i+1, j} - P_{\sigma, i-1, j}}{2h}, \\ \partial_{k_y} P_\sigma(\mathbf{k}) &\approx \frac{P_{\sigma, i, j+1} - P_{\sigma, i, j-1}}{2h}. \end{aligned}$$

Thus, in equation (B1) we simplify

$$\begin{aligned} &P_\sigma(\mathbf{k}) \left[\partial_{k_x} P_\sigma(\mathbf{k}), \partial_{k_y} P_\sigma(\mathbf{k}) \right] \\ &\approx \frac{P_{\sigma, i, j}}{4h^2} \left([P_{\sigma, i+1, j}, P_{\sigma, i, j+1}] + [P_{\sigma, i, j+1}, P_{\sigma, i-1, j}] \right. \\ &\quad \left. + [P_{\sigma, i-1, j}, P_{\sigma, i, j-1}] + [P_{\sigma, i, j-1}, P_{\sigma, i+1, j}] \right). \end{aligned}$$

Note that due to periodic boundary conditions in BZ, $P_{\sigma, L_x+1, j} \equiv P_{\sigma, 1, j}$ and $P_{\sigma, i, L_y+1} \equiv P_{\sigma, i, 1}$. Then the

Chern number is approximated as

$$\begin{aligned}
C_\sigma &= \frac{1}{2\pi i} \int_{\text{B.Z.}} \text{Tr} (P_\sigma dP_\sigma \wedge dP_\sigma) \\
&\approx \frac{1}{2\pi i} \sum_{i,j=1}^N \frac{P_{\sigma,i,j}}{4} \left([P_{\sigma,i+1,j}, P_{\sigma,i,j+1}] + [P_{\sigma,i,j+1}, P_{\sigma,i-1,j}] \right. \\
&\quad \left. + [P_{\sigma,i-1,j}, P_{\sigma,i,j-1}] + [P_{\sigma,i,j-1}, P_{\sigma,i+1,j}] \right). \quad (\text{B4})
\end{aligned}$$

Under such a construction, the evaluation of the spin Chern number might be subject to finite-size effects and an integral Chern number is not guaranteed. However, as we have presented in this paper, the approach is still useful in characterizing topological phase transitions which involve Chern number variations.